

Research Article

Investigation on Low Frequency Bandgap of Coupled Double Beam with Quasi-Zero Stiffness for Power Transformer Vibration Control

Qiang He ,¹ Jingkai Nie,¹ Yu Han,¹ Yi Tian,¹ Chao Fan,¹ and Guangxu Dong ²

¹State Key Laboratory of Advanced Power Transmission Technology, State Grid Smart Grid Research Institute Co. Ltd., Beijing 102201, China

²Institute of Sound and Vibration Research, Hefei University of Technology, Hefei 230009, China

Correspondence should be addressed to Guangxu Dong; d865290612@163.com

Received 12 August 2022; Revised 19 November 2022; Accepted 25 November 2022; Published 31 December 2022

Academic Editor: Vasudevan Rajamohan

Copyright © 2022 Qiang He et al. This is an open access article distributed under the Creative Commons Attribution License, which permits unrestricted use, distribution, and reproduction in any medium, provided the original work is properly cited.

To suppress low frequency vibration and noise generated by power transformer in residential area and achieve environment protection standards, a double-beam metamaterial is proposed, which is fabricated through periodically coupling silicon steel sheet and aluminum beams with Belleville quasi-zero stiffness spring (BQZSS). The double-beam metamaterial can be assembled with iron core of transformers as a whole to obtain the design of a low-noise transformer. Performing static analysis, the mechanical model of BQZSS is established and the relationship between restoring force, stiffness, and displacement can be obtained. Then, the mechanical properties of BQZSS are verified with the finite element method. On this basis, the governing equations of the unit cell of the double-beam metamaterial are derived using Euler–Bernoulli beam theory. According to Bloch theorem and boundary conditions, the dispersion relation of the double-beam metamaterial is deduced, and behaviors of flexural wave propagation in beams are investigated. The effects of structure parameters on bandgaps and dispersion properties are studied, and the low frequency vibration bandgap mechanism is revealed. Finally, the frequency response function (FRF) of the double-beam metamaterial with a finite length is calculated in ANSYS to verify the bandgap characteristics given by a theoretical model. The results show that the double-beam metamaterial can yield multiple low frequency bandgaps at 100 Hz, 200 Hz, 300 Hz, and 500 Hz for suppression of flexural vibration components of transformers, which benefits from Bragg scattering (BS) and the blend of BS and LR mechanisms. The opening and closing of the low frequency bandgaps and the attenuation constants within bandgaps can be tuned by choosing parameters of beams. These findings suggest that the coupling between beams can lead to novel dispersion properties, which provides a new control approach for low frequency vibration and noise in power transformer.

1. Introduction

With the rapid development of urbanization, urban electricity consumption has increased significantly and corresponding voltage level of power transmission and transformation equipment has increased accordingly. As a result, the high-voltage transmission lines have been brought in the center of cities, and many high-voltage and large-capacity transformers have been mounted in residential areas [1]. While transformers offer the convenience for high-voltage transmission, the low frequency vibration and noise generated by silicon steel sheets of iron core of transformers

poses a severe challenge to environmental standards. The low frequency vibration and noise of transformers has been recognized as the main pollution source of residents near power plants, substations, and converter stations, and this kind of pollution becomes more and more serious with the continuous improvement of transmission capacity and voltage level [2]. The low frequency vibration and noise of iron core of transformers due to magnetostriction occur twice per a current cycle. Thus, for operating frequency at 50 Hz, the vibration and noise of transformers mainly consists of 100 Hz and its harmonics (200 Hz, 300 Hz, and so on) [3]. These low frequency vibration and noise will not

only adversely affect the operation of equipment but also degrade the comfort of residents. Note that the low frequency vibration and noise has high diffraction ability and wide propagation distance, which can make people's blood pressure rise, become irritable, and even lose their sense of mind [4–6]. With the increasingly stringent environmental regulations, the low frequency vibration and noise of transformers have become an important factor that cannot be ignored in high-voltage power transmission. Hence, how to reduce the low frequency vibration and noise of transformers is an urgent problem to be solved.

Up to now, investigations on controlling low frequency vibration and noise of transformers mainly focus on noise source control, propagation path control, and receiver protection [7], such as selecting silicon steel sheet with small magnetostriction to reform transformer body, installing sound barriers for transformer, and using active noise control methods for noise cancellation [8]. Using 27ZDKH silicon steel sheet to replace traditional ones, Wang and Zhao [9] designed a new transformer iron core and the magnetic flux in iron core has been reduced from 1.75 T to 1.5 T, the noise of transformer is dropped by 5 dB. To control propagation path, Hu et al. [10] took 220 kV transformers as an object to investigate the performance of sound insulation of sound barriers, and results show that noise can be reduced by 1 dB. Liu et al. [11] adopted single and double microperforated panels (MPPs) to mitigate noise pollution of transformers, and results reveal that the sound pressure level reduction is about 3 and 4.6 dB after installing single and double MPPs. To achieve ventilation and heat dissipation on the propagation path, coiled-up silencers consisting of coupled tubes was designed by Wang et al. [12] to offer both air circulation and noise reduction for transformers. As active noise control (ANC) is good at low frequency problem, combining with active feedforward control algorithm, Zhang et al. [13] employed microphone array to conduct the active noise control, and then the simulations indicate that the low frequency noise components at frequencies 50 Hz, 100 Hz, and 200 Hz are attenuated by 12–18 dB. Zhao et al. [14] developed a new FXLMS algorithm for active noise control of transformers, and this active system can obtain noise reduction of 8–15 dB. Although the abovementioned approaches can obtain considerable noise reduction for transformers, they are always limited in practice. Especially for ferromagnetic material with small magnetostriction is expensive. As for noise barrier and microperforated panel, they not only occupy a large space but also cause difficulties in heat dissipation and daily maintenance of transformers. In addition, the active noise control always requires multiple secondary sound sources and complex control algorithm.

In comparison with reforming transformer, sound barrier, and active noise control, the noise reduction based on vibration control of transformer structure has also been paid more attention. Once the vibration of transformers is reduced, the sound radiation of the equipment will be reduced to a certain extent. Thus, researchers design various vibration isolators or absorbers installed on the propagation path of vibration and noise of transformers. Supporting

transformer with rubber isolators, Zhang [15] performed sound radiation analysis of transformer and pointed out that the rubber isolator can decrease the sound radiation. Dong et al. [16] adopted magnetic negative stiffness spring in parallel with folding beam to construct a quasi-zero stiffness transformer isolation platform with friction damping, and the simulation shows that the platform can effectively suppress the low frequency vibration and noise of the transformer. Moreover, the nonlinear damping was also added to quasi-zero stiffness isolator for resonance suppression of transformer [17]. Recently, Zhou et al. [18] employed vertical and inclined springs to devise a quasi-zero stiffness isolator for transformer and the experimental results show that the isolator can effectively suppress low frequency vibration of the transformer, thus, the sound radiation can be reduced. Besides that, Cao et al. [19] studied the vibration and noise suppression of transformers attached with tuned mass damper (TMD) and the results show that the maximum noise reduction of TMD is close to 1.6 dB (A). Although the abovementioned can achieve transformer noise reduction, whereas the rubber isolator will be aged and lose performance due to high temperature of transformer, and for quasi-zero stiffness isolator and TMD, they are limited in application because of their large dimensions.

According to the investigations reviewed above, it is hard for traditional material and vibration attenuation structures to suppress low frequency vibration and noise of transformers. Therefore, it is necessary to explore new ways to cope with the low frequency vibration and noise of transformers. Recently, the subwavelength photonic crystals and acoustic metamaterial have become the hot topic because of their advantages in low frequency vibration and noise control, such as high tunability and small volume. Referring to Hilbert fractal curve, Wang et al. [20] exploited the labyrinth structure to design acoustic metamaterial for transformers, and the experimental results show that its sound transmission loss can reach up to 20 dB in the range from 100 Hz to 800 Hz, respectively. Similarly, Zhao et al. [21] designed a hybrid coil-type acoustic metamaterial for suppressing audible noise of transformers at 400 Hz and 500 Hz, and the sound transmission loss in the bandgap from 400 Hz to 500 Hz reaches 25 dB. Furthermore, considering high-order Hilbert fractal curves, the sound transmission loss of third-order acoustic metamaterials can reach more than 30 dB at the main frequencies of transformer noise [22]. In addition to Hilbert fractal form, maze-like acoustic metamaterial [23] was also employed by Zhao to obtain sound transmission loss about 25 dB in the frequency band of 100 Hz–500 Hz. Although the Hilbert fractal, labyrinth, coil-type, and maze-like acoustic metamaterial can realize great noise reduction, the acoustic diffraction along the edges of Hilbert fractal acoustic metamaterial decreases the overall noise reduction. Thus, Wang et al. [24] combined ANC with the Hilbert fractal acoustic metamaterial to counteract the diffracting sound waves of transformers near the edges of the metamaterial, and the results show that the sound pressure level with ANC on the specified points is more than 10 dB lower than that without ANC. As thin film metamaterials have advantages in low

frequency bands, Yuchao et al. [25] developed a membrane-type acoustic metamaterial to attenuate the noise of transformers in the frequency range from 100 Hz to 500 Hz. To absorb multiple low frequency components of transformer noise, Sharafkhani [26] connected multiple Helmholtz resonators in series and parallel to obtain the perfect sound absorption at frequencies 100 Hz, 200 Hz, and 300 Hz, respectively. Ye et al. [27] proposed a step-by-step structural design method to design plate-type acoustic metamaterial for transformers, which can address single-frequency and multifrequency sound insulation. Although the above-mentioned acoustic metamaterial can effectively attenuate the low frequency vibration and noise of transformer, these metamaterial can only be mounted outside of the transformer and occupy too much space. Hence, developing the new form of metamaterial applied to control low frequency vibration and noise of transformer is urgent.

As is known to all, the low frequency vibration and noise of transformer is mainly attributed to the magnetostriction, which results in flexural vibration of silicon steel sheets under AC magnetic flux [2]. Thus, suppressing the low frequency flexural vibration of silicon steel sheet will be a new choice to reduce the sound radiation of transformer. Hence, by periodically coupling silicon steel sheet and aluminum with BQZSS, this paper proposes a double-beam metamaterial to attenuate the low frequency flexure vibration of silicon steel sheet. Subsequently, the low frequency noise radiated from transformers would be reduced accordingly. The double-beam metamaterial yields multiple low frequency bandgaps to attenuate the low frequency vibration and noise of transformers at 100 Hz, 200 Hz, 300 Hz, and 500 Hz, and can be assembled with iron core of transformers as a whole to obtain the design of the low-noise transformer. So that the drawbacks of large space occupation and difficulties in heat dissipation and maintenance of transformers can be overcome. Unlike the traditional Bragg scattering or local resonance metamaterial using lattice or discrete resonators, the multiple low frequency bandgaps of the double-beam metamaterial are formed with dynamic coupling created by BQZSS, while each beam does not individually have bandgap.

The rest of this paper is organized as follows: In Section 2, both the physical and mechanical models of the double-beam metamaterial and BQZSS are presented. The dispersion relationship and bandgap structures are investigated in Section 3. In Section 4, numerical simulations and analysis of double-beam metamaterial are conducted. Finally, conclusions are summarized in Section 5.

2. Double-Beam Metamaterial with BQZSS

2.1. Conceptual Model of the Double-Beam Metamaterial with Quasi-Zero Stiffness. The layout of transformer iron core is presented in Figure 1, which is composed of silicon steel sheets and double-beam metamaterial. Connecting four silicon steel sheet beams end-to-end and then stacking silicon steel sheet beams into square form, the square iron core of transformer can be obtained. Once alternating current is applied to the windings wound on square iron core, the

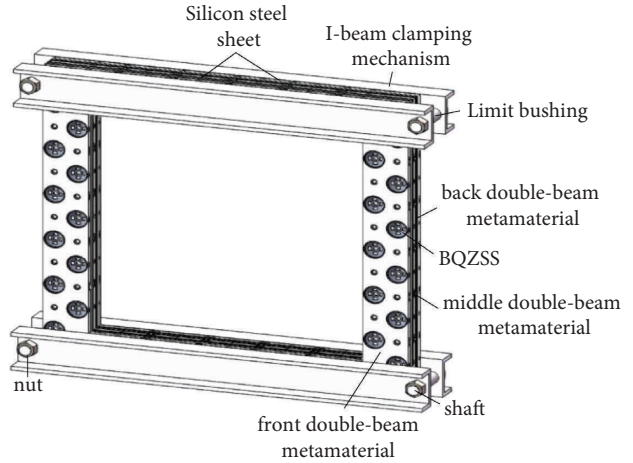


FIGURE 1: Transformer iron core with silicon steel sheets and double-beam metamaterial.

magnetostriction of silicon steel sheet under time-varying magnetic flux occurs, which results in the low frequency bending vibration of silicon steel sheets along with normal direction of its surface. Thus, the low frequency sound radiation would be generated due to the low frequency bending vibration of silicon steel sheet, and subsequently, the environmental pollution is produced. In order to suppress these low frequency vibration and noise, the double-beam metamaterials are respectively installed at the front, middle, and back ends of square silicon steel sheets. The square silicon steel sheets and double-beam metamaterial are clamped and assembled together using I-beam clamping mechanisms, and the nuts and limit bushings are employed to offer preload for iron core. As configured in such a form, the low frequency flexural vibration of square silicon steel sheets can be attenuated by double-beam metamaterial.

As shown in Figure 2, the double-beam metamaterial consists of one group of front and back beams, which are connected end-to-end to form the square. Each group of double-beam is composed of silicon steel sheet beam and aluminum beam, and a number of BQZSSs are uniformly distributed between two beams with equal space. To make BQZSS operate at its equilibrium position, a preload of $400 \text{ N} \sim 600 \text{ N}$ is applied on I-beam clamping mechanisms by screwing nuts along with limit bushing. Thus, the dynamic coupling between the silicon steel sheet and aluminum beams is created by BQZSS, which can produce low frequency vibration bandgaps for transformer vibration and noise control.

Referring to the iron core of power transformer displayed in Figures 1 and 2 and for the convenience of following analysis, the double-beam metamaterial is further simplified to the mechanical model in Figure 3(a), and one unit cell of length L containing two beams and two BQZSSs are presented in Figure 3(b). Two BQZSSs shown in Figure 4 are compressed with each other to provide coupling for two beams.

2.2. Static Analysis of Belleville Quasi-Zero Stiffness Spring. To suppress the low frequency vibration and noise of transformer, the mechanical properties of BQZSS should be

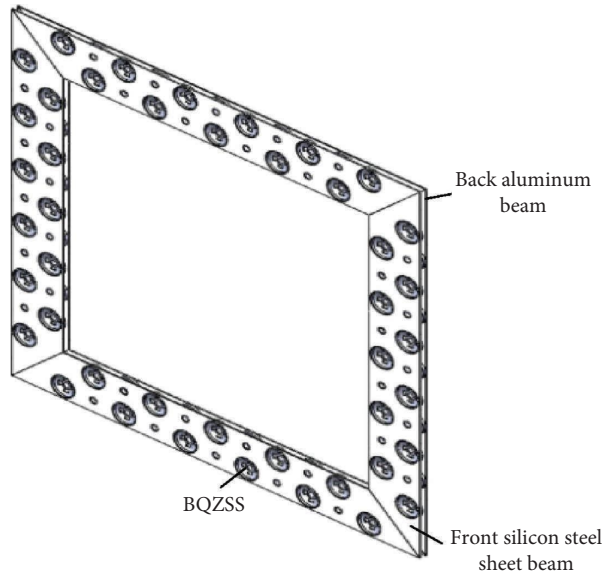


FIGURE 2: Double-beam metamaterial.

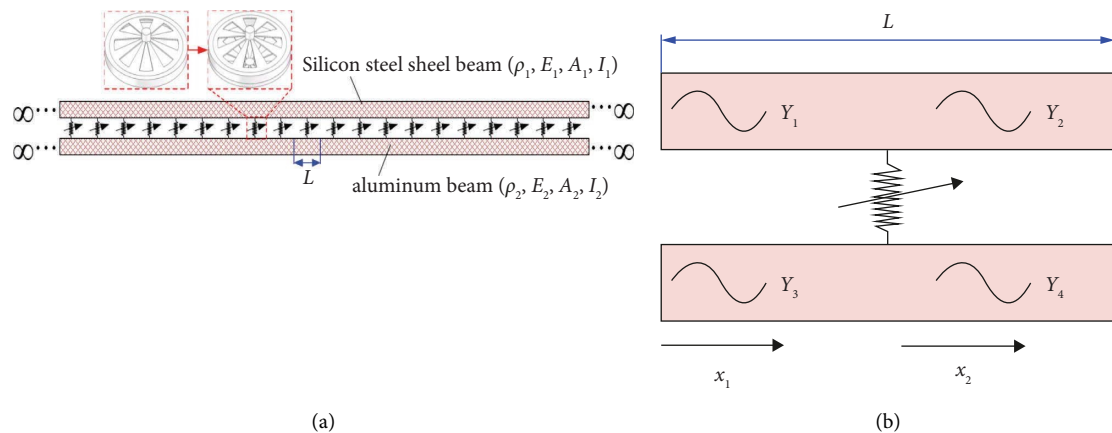


FIGURE 3: Double-beam metamaterial: (a) mechanical model of double-beam metamaterial and (b) unit cell of double-beam metamaterial.

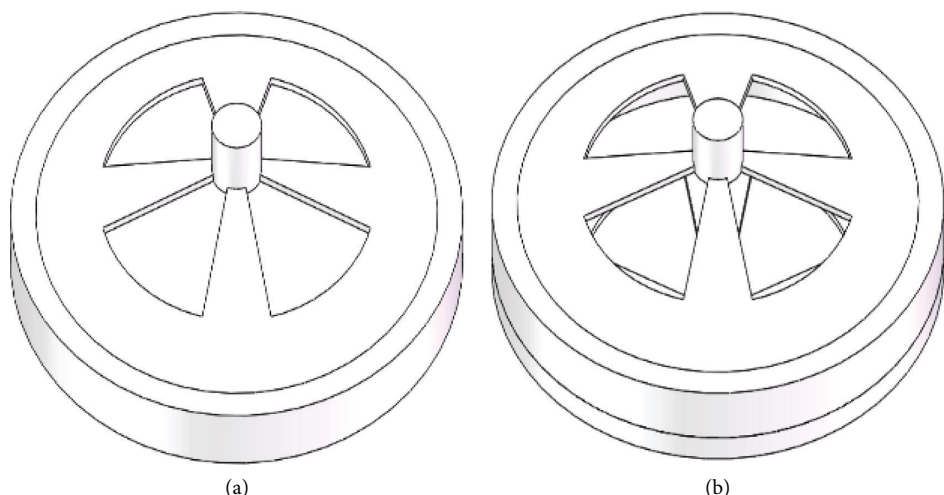


FIGURE 4: BQZSS: (a) single BQZSS and (b) two counter-pressure springs.

analyzed since the coupling is generated by BQZSS. Figure 5 shows the dimensions of BQZSS. There are four slots existing in BQZSS's conical surface. As can be seen from Figure 5, b_1 and b_2 are the widths of tips of the slots, D_m is the diameter of bottom circle of the slot, d is the diameter of tip circle of slot, h is the height of closed conical surface, D is the diameter of bottom of BQZSS, t is the thickness of BQZSS, and L_0 is the height of BQZSS. When an external force F_n is applied on the top of BQZSS, the corresponding deformation is displayed in Figure 5(c). It should be noted that the overall displacement δ of the top of BQZSS in vertical direction is contributed by two parts: one is the flexural displacement δ_1 that comes from closed conical surface, and the other is the bending deformation δ_2 which is attributed to elastic deformation of slotted parts.

In terms of the elastic theory [28], the relationship between the external force F_n and displacement δ_1 can be expressed as follows:

$$F_n = \frac{E}{1-\mu^2} \cdot \frac{t^3}{D^2} \cdot K_1 \delta_1 \left[1 + \left(\frac{h}{t} - \frac{\delta_1}{t} \right) \left(\frac{h}{t} - \frac{\delta_1}{2t} \right) \right] \left[\frac{(1-D_m/D)}{(1-d/D)} \right], \quad (1)$$

where E and μ are elastic modulus and Poisson's ratio of the material of BQZSS, separately. It is clear that F_n in equation

$$k_{qzs} = \frac{(EtK_1[t^2 + (h - \delta_1)(h - \delta_1/2)](1 - D_m/D)/(1 - \mu^2)D^2(1 - d/D)) - (EtK_1\delta_1(3h - 2\delta_1)(1 - D_m/D)/2(1 - \mu^2)D^2(1 - d/D))}{D - d/D - D_m + (C(D_m - d)^3(1 - \mu^2)/2Et^3b_2Z) \cdot [EtK_1[t^2 + (h - \delta_1)(h - \delta_1/2)](1 - D_m/D)/(1 - \mu^2)D^2(1 - d/D) - EtK_1\delta_1(3h - 2\delta_1)(1 - D_m/D)/2(1 - \mu^2)D^2(1 - d/D)]}. \quad (5)$$

To verify the effectiveness of the restoring force of BQZSS given in equation (1), the finite element model of BQZSS is established using ANSYS software as shown in Figure 6. During the finite element analysis, the solid 185 element is adopted to model BQZSS and swept mesh is then generated. Herein, we use Nylon PA12 to fabricate BQZSS, and their structural parameters are listed in Tables 1 and 2. In Figure 6(c), the displacement of all nodes located at the bottom of BQZSS in X, Y, and Z directions is set to 0, and the displacement of all nodes on the top of BQZSS is coupled together. Only the vertical displacement of the coupling nodes on the top of BQZSS is allowed. To obtain the nonlinear characteristics of BQZSS, the displacement load is imposed on the coupling nodes and then the reaction force of coupling nodes can be obtained.

As displayed in Figure 7, the results of restoring force calculated by equation (1) are compared with that computed by ANSYS software. The restoring force of BQZSS around its equilibrium position is about 450 N, which can be employed to preload iron core of transformer. Most importantly, the restoring force curves around the equilibrium position are so flat that they can be substituted with constant for following analysis. As can be seen from the comparison, the theoretical restoring force given by equation (1) has a good agreement with that obtained by finite element ones, which has verified the theoretical model.

Referring to equation (5), the stiffness expression is so complicated that it is inconvenient for following analysis.

(1) is the function of displacement δ_1 and the structural dimensions of BQZSS. Note that the relationship between the overall displacement δ , bending deformation δ_2 , and flexural displacement δ_1 can be expressed as follows:

$$\delta_2 = \frac{C(D_m - d)^3(1 - \mu^2)F_n}{2Et^3b_2Z}, \quad (2)$$

$$\delta = \left[\frac{(1 - d/D)}{(1 - D_m/D)} \right] \delta_1 + \delta_2, \quad (3)$$

where Z is the slot number and coefficients K_1 and C are given by

$$K_1 = \frac{2\pi}{3} \cdot \frac{(D/D_m)^2 \ln(D/D_m)}{[D/D_m - 1]^2}, \quad (4)$$

$$C = \frac{3}{(1 - b_1/b_2)^3} \left[\frac{1}{2} - 2 \frac{b_1}{b_2} + \left(\frac{b_1}{b_2} \right)^2 \left(\frac{3}{2} - \ln \frac{b_1}{b_2} \right) \right].$$

According to equations (1)–(3), differentiating force F_n in equation (1) with respect to overall displacement δ yields the stiffness of BQZSS as follows:

$$K_{qzs}(\delta) = k_1 \delta + k_3 \delta^3, \quad (6)$$

where k_1 and k_3 are the approximate stiffness coefficients, and they are listed in Table 3. The stiffness results calculated by equations (5) and (6) are compared in Figure 8. In the range of 0 to 8 mm, the stiffness of BQZSS calculated with equation (5) is in good agreement with that given by Taylor approximation in equation (6), and nonlinearity of three stiffness curves around equilibrium position is so weak that the stiffness around equilibrium can be approximated as a constant for following analysis. Subsequently, the linear stiffness term k_1 in equation (6) will be used to carry out the analysis of bandgap structures of double-beam metamaterial.

3. Propagation of Flexural Waves in Double-Beam System and Wave Dispersion

Referring to the mechanical model of double-beam metamaterial in Figure 3(a), the system consists of two uniform beams periodically coupled with BQZSS that enforce the continuity of transverse displacement and rotation at the connection points between the two beam elements. The dynamics of double-beam metamaterial is investigated by

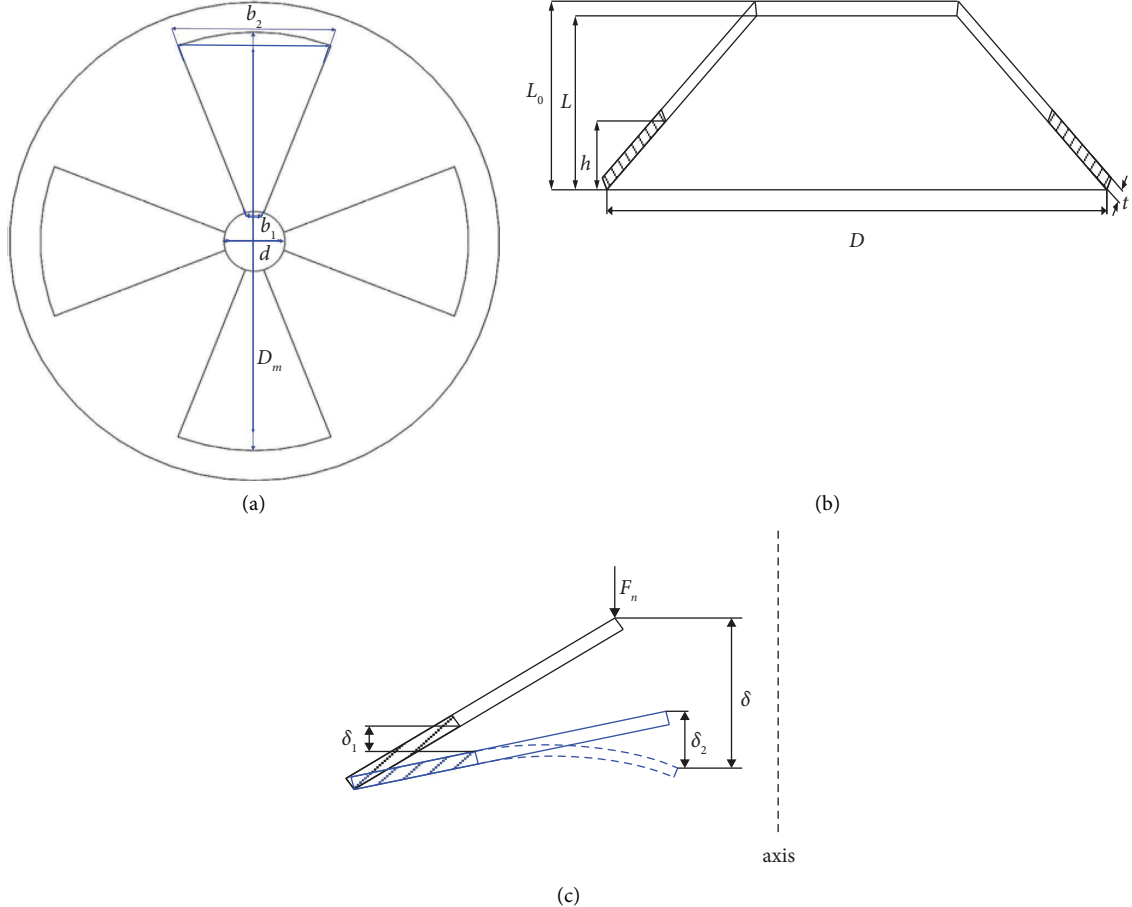


FIGURE 5: Mechanical model of BQZSS: (a) vertical view, (b) front view, and (c) deformation of BQZSS.

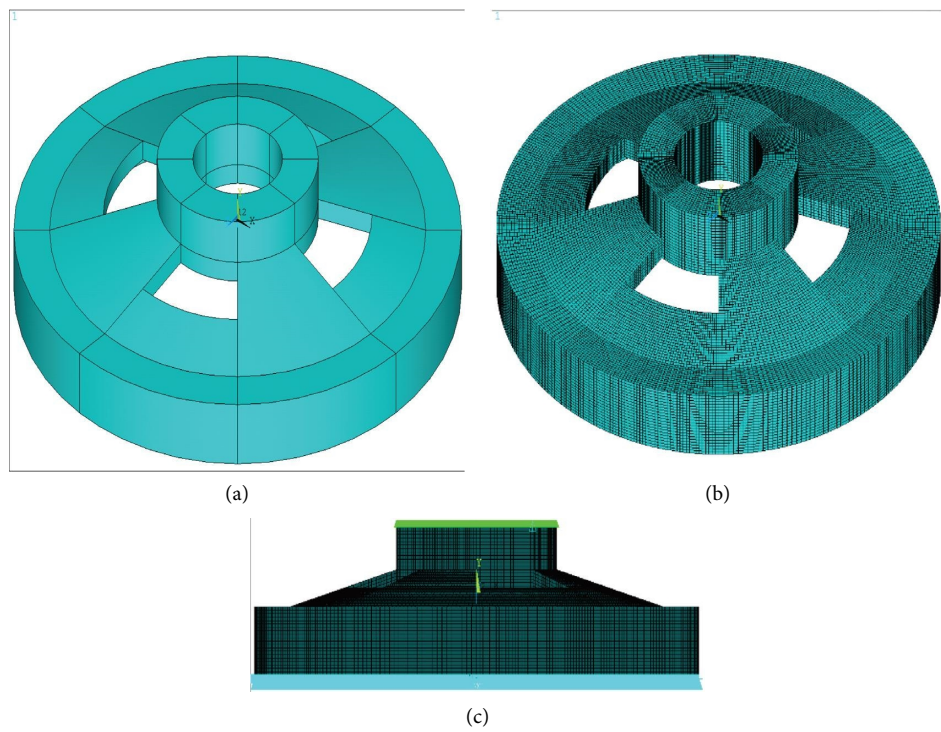


FIGURE 6: Finite element model of BQZSS: (a) entity model, (b) finite element model, and (c) constraint conditions.

TABLE 1: Mechanical parameters of BQZSS.

Name	Elastic modulus (E)	Poisson's ratio (μ)	Density (ρ)
PA12	1.3 Gpa	0.4	1150 kg/m ³

TABLE 2: Dimensions of BQZSS.

Names	b_1	b_2	d	D_m	D	L_0	L	h	t
PA12-I	7.0	11	19	31	49	13	10	3.5	4
PA12-II	7.0	12	19	33	49	13	10	3.3	4
PA12-III	7.0	13	19	35	49	13	10	3.0	4

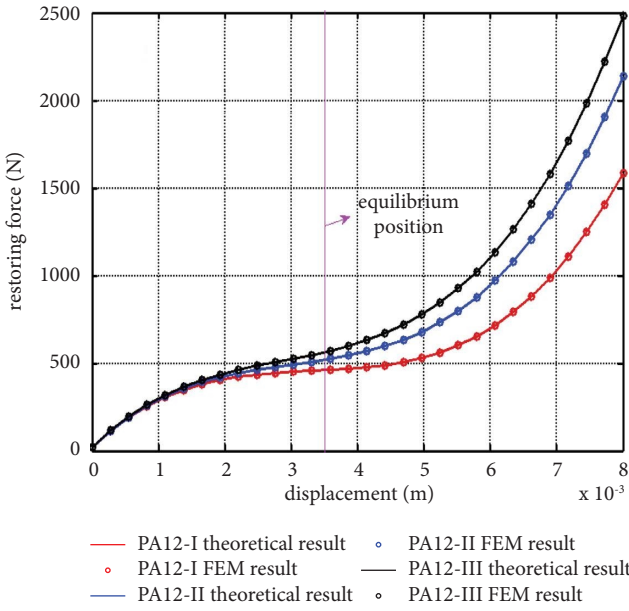


FIGURE 7: Restoring force of BQZSS.

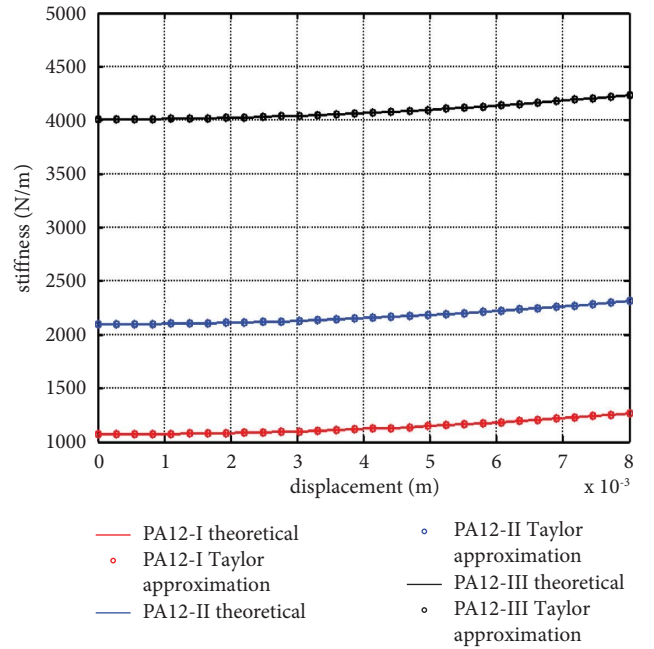


FIGURE 8: Stiffness of BQZSS.

TABLE 3: Coefficients of Taylor approximation.

Names	k_1 (N·m ⁻¹)	K_3 (N·m ⁻¹)
PA12-I	1035	2.9982e6
PA12-II	2092	3.2527e6
PA12-III	4150	3.4481e6

deriving the governing equations for one of its unit cells in Figure 3(b). Setting up local coordinate systems $x_1 \circ y_1$, $x_1 \circ y_3$, $x_2 \circ y_2$, and $x_2 \circ y_4$, the vibration displacement of each beam can be expressed as $Y_1(x_1, t)$, $Y_2(x_2, t)$, $Y_3(x_1, t)$, and $Y_4(x_2, t)$, respectively.

3.1. Dispersion Relation. Following the Euler–Bernoulli beam theory and assuming that the coupling of the two beams is exactly imposed in the middle of unit cell. The governing equations are written as follows:

$$\frac{\partial^2}{\partial x_1^2} \left(E_1 I_1 \frac{\partial^2 Y_1(x_1, t)}{\partial x_1^2} \right) + \rho_1 A_1 \frac{\partial^2 Y_1(x_1, t)}{\partial t^2} = 0, \quad (7)$$

$$\frac{\partial^2}{\partial x_2^2} \left(E_1 I_1 \frac{\partial^2 Y_2(x_2, t)}{\partial x_2^2} \right) + \rho_1 A_1 \frac{\partial^2 Y_2(x_2, t)}{\partial t^2} = 0, \quad (8)$$

$$\frac{\partial^2}{\partial x_1^2} \left(E_2 I_2 \frac{\partial^2 Y_3(x_1, t)}{\partial x_1^2} \right) + \rho_2 A_2 \frac{\partial^2 Y_3(x_1, t)}{\partial t^2} = 0, \quad (9)$$

$$\frac{\partial^2}{\partial x_2^2} \left(E_2 I_2 \frac{\partial^2 Y_4(x_2, t)}{\partial x_2^2} \right) + \rho_2 A_2 \frac{\partial^2 Y_4(x_2, t)}{\partial t^2} = 0, \quad (10)$$

where E_1 , E_2 , ρ_1 , ρ_2 , A_1 , A_2 , I_1 , and I_2 refer to Young's modulus, density, cross-sectional area, and moment of inertia of two beams. Considering the travelling wave solution, the solutions of equations (7)–(10) can be written as follows:

$$\begin{aligned} Y_1(x_1, t) &= y_1(x_1)e^{i\omega t}, \\ Y_2(x_2, t) &= y_2(x_2)e^{i\omega t}, \\ Y_3(x_1, t) &= y_3(x_1)e^{i\omega t}, \\ Y_4(x_2, t) &= y_4(x_2)e^{i\omega t}, \end{aligned} \quad (11)$$

where the general solutions $y_1(x_1)$, $y_2(x_2)$, $y_3(x_1)$, and $y_4(x_2)$ are given by

$$y_1(x_1) = a_{11} \cos \frac{\sqrt{\omega}}{\beta_1} x_1 + a_{12} \sin \frac{\sqrt{\omega}}{\beta_1} x_1 + a_{13} \cosh \frac{\sqrt{\omega}}{\beta_1} x_1 + a_{14} \sinh \frac{\sqrt{\omega}}{\beta_1} x_1, \quad (12)$$

$$y_2(x_2) = a_{21} \cos \frac{\sqrt{\omega}}{\beta_1} x_2 + a_{22} \sin \frac{\sqrt{\omega}}{\beta_1} x_2 + a_{23} \cosh \frac{\sqrt{\omega}}{\beta_1} x_2 + a_{24} \sinh \frac{\sqrt{\omega}}{\beta_1} x_2, \quad (13)$$

$$y_3(x_1) = a_{31} \cos \frac{\sqrt{\omega}}{\beta_2} x_1 + a_{32} \sin \frac{\sqrt{\omega}}{\beta_2} x_1 + a_{33} \cosh \frac{\sqrt{\omega}}{\beta_2} x_1 + a_{34} \sinh \frac{\sqrt{\omega}}{\beta_2} x_1, \quad (14)$$

$$y_4(x_2) = a_{41} \cos \frac{\sqrt{\omega}}{\beta_2} x_2 + a_{42} \sin \frac{\sqrt{\omega}}{\beta_2} x_2 + a_{43} \cosh \frac{\sqrt{\omega}}{\beta_2} x_2 + a_{44} \sinh \frac{\sqrt{\omega}}{\beta_2} x_2, \quad (15)$$

where $\beta_i = \sqrt[4]{E_i I_i / \rho_i A_i}$ ($i = 1, 2$). There are sixteen unknown coefficients a_{jk} ($j = 1 \sim 4$, $k = 1 \sim 4$) existing in equations (12)–(15), and they can be determined by imposing the boundary conditions. As shown in Figure 3(b), the first set of boundary conditions is the continuity of displacements and balance of forces within each beam element:

$$y_1\left(\frac{L}{2}\right) = y_2(0), \quad (16)$$

$$\theta_1\left(\frac{L}{2}\right) = \theta_2(0), \quad (17)$$

$$y_3\left(\frac{L}{2}\right) = y_4(0), \quad (18)$$

$$\theta_3\left(\frac{L}{2}\right) = \theta_4(0), \quad (19)$$

$$-Q_1\left(\frac{L}{2}\right) + Q_2(0) + f_s = 0, \quad (20)$$

$$-Q_3\left(\frac{L}{2}\right) + Q_4(0) - f_s = 0, \quad (21)$$

$$-M_1\left(\frac{L}{2}\right) + M_2(0) = 0, \quad (22)$$

$$-M_3\left(\frac{L}{2}\right) + M_4(0) = 0, \quad (23)$$

where $\theta_i = dy_i/dx_i$ ($i = 1, 2$) is angle, and $M_i = E_i I_i d^2 y_i / dx_i^2$ and $Q_i = dM_i / dx_i$ denote the moment and shear force in two beams. In equations (20) and (21), f_s is the force offered by two BQZSSs and can be defined as follows:

$$f_s = \frac{k_1}{2} [y_2(0) - y_4(0)]. \quad (24)$$

The second set of boundary conditions is coming from the Bloch theorem:

$$y_2\left(\frac{L}{2}\right) = y_1(0)e^{-iqL}, \quad (25)$$

$$\theta_2\left(\frac{L}{2}\right) = \theta_1(0)e^{-iqL}, \quad (26)$$

$$y_4\left(\frac{L}{2}\right) = y_3(0)e^{-iqL}, \quad (27)$$

$$Q_2\left(\frac{L}{2}\right) = Q_1(0)e^{-iqL}, \quad (28)$$

$$\theta_4\left(\frac{L}{2}\right) = \theta_3(0)e^{-iqL}, \quad (29)$$

$$M_2\left(\frac{L}{2}\right) = M_1(0)e^{-iqL}, \quad (30)$$

$$Q_4\left(\frac{L}{2}\right) = Q_3(0)e^{-iqL}, \quad (31)$$

$$M_4\left(\frac{L}{2}\right) = M_3(0)e^{-iqL}, \quad (32)$$

Substituting solutions in equations (12)–(15), into the boundary conditions (16)–(30), then a set of algebraic equations can be obtained. Setting the determinant of the coefficient matrix to zero, the dispersion relation is determined in the following form:

$$(e^{4\mu} + e^{-4\mu}) + T_1(e^{3\mu} + e^{-3\mu}) + T_2(e^{2\mu} + e^{-2\mu}) + T_3(e^{\mu} + e^{-\mu}) + T_4 = 0, \quad (33)$$

where $\mu = iqL$, $i = \sqrt{-1}$, q is the wave vector and coefficient T_j ($j = 1 \sim 4$) is listed in Appendix A. As $\cosh \mu = \cos(iqL)$, the

$$\cos^4(iqL) + \frac{T_1}{2}\cos^3(iqL) + \frac{T_2 - 4}{4}\cos^2(iqL) + \frac{T_3 - 3T_1}{8}\cos(iqL) + \frac{T_4 - 2T_2 + 2}{16} = 0. \quad (34)$$

It is clear that equation (34) is a quartic algebraic equation in $\cos qL$. Hence, four pairs of wave solutions $\pm q_1$, $\pm q_2$, $\pm q_3$, and $\pm q_4$ exist for a given frequency ω , and each pair waves represent the same characteristic wave but travels in opposite directions. According to the expression of four pairs of wave solutions, the flexural wave can be divided into following three categories [29]:

- (i) *Propagating*. The wave number is real (i.e., $q = \text{Re}(q)$). The flexural wave travels through the unit cell without attenuation.
- (ii) *Attenuating*. The imaginary part of wave number is nonzero and the real part is 0 or π . The flexural wave will be attenuated when travelling cross the unit cell.
- (iii) *Complex*. The wave number q is complex (i.e., $0 < \text{Re}(q) < \pi$ and $\text{Im}(q) > 0$). The flexural wave is attenuating when it travels through the unit cell.

As a result, it all depends on what kind of wave number q is, the double-beam metamaterial may have three types of bandgap properties for flexural wave attenuation at a given frequency ω :

- (a) *Attenuation-Attenuation-Attenuation-Attenuation*. All wave numbers belong to the attenuating category. The two adjacent cells vibrate either in phase or out of phase, and all waves will be attenuated as they travel through the unit cell. This phenomenon is attributed to Bragg scattering. Hence, this bandgap is called as Bragg scattering (BS) zone.
- (b) *Complex-Complex-Complex-Complex*. Four pairs of wave numbers belong to category (III), and are complex-conjugate. Four pairs of wave numbers denote the same characteristic wave that attenuate and experience a phase change when they travel across a unit cell. This is typical local resonance. Therefore, this bandgap can be marked as local resonance (LR) zone.
- (c) *Complex/Attenuating*. At least one pair of wave number belongs to BS, and the others are LR types. Thus, all waves will be attenuated as they travel cross unit cell whereas this type of attenuation benefits from the blend of BS and LR mechanisms.

Based on the analysis conducted above, three types of bandgaps may be generated by the double-beam metamaterial. In the next subsection, we will investigate the

dispersion relation in equation (33) can be written as follows:

bandgap structures and dispersion properties of the double-beam metamaterial.

3.2. Bandgap Structure of Double-Beam Metamaterial. According to the mechanical characteristics of BQZSS studied in Section 2.2, the stiffness of BQZSS given in equation (6) is nonlinear, whereas the restoring force and stiffness curves plotted in Figures 7 and 8 are so flat around equilibrium position that the stiffness can be linearized. For convenience, the stiffness of BQZSS around its equilibrium position is approximated with constant k_1 . Hence, the stiffness contained in unit cell is $k_1/2$ in Figure 3(b). The parameters of silicon steel sheet and aluminum beams for simulation are listed in Table 4.

First of all, the Taylor approximation of stiffness of BQZSS made of PA12-I is utilized to study the bandgap structures and dispersion properties of the double-beam metamaterial. Refer to the dispersion relation given by equation (34) and the parameters of beams listed in Table 4, the wave vector qL can be obtained by calculating equation (34), and then, the real and imaginary parts are exhibited in Figures 9(a) and 9(b), respectively. These curves show that within the third bandgap, all wave number solutions are of Attenuation-Attenuation-Attenuation-Attenuation type, which is consistent with Bragg scattering mechanism. Compared with the third bandgap, the behavior of wave number varies when the wave travels crossing the first, second, and fourth bandgaps. These bandgaps possess two Complex and two Attenuating wave number pairs, and all of wave number solutions are Attenuating type as the frequency increases. Hence, the first, second, and fourth bandgaps benefit forms the blend of BS and LR mechanisms.

Note that the real part of wave numbers determines the dispersion properties of propagating waves, while the imaginary part of wave numbers governs the attenuation properties of the double-beam metamaterial. Keeping this in mind, the bandgap structures in Figures 9(a) and 9(b) can be simplified into the representation in Figures 9(c) and 9(d). As can be seen from Figure 9(c), four bandgaps exist in the frequency range of 0 Hz to 1000 Hz. The first bandgap spans from 73.34 Hz to 115.3 Hz, and wave numbers within this bandgap are two Complex and two Attenuating types. Similarly, the second and fourth bandgaps are from 150.3 Hz/487.4 Hz to 214.8 Hz/516.4 Hz. The first, second,

TABLE 4: Physical parameters of beams.

Names	Elastic modulus (E)	Density (ρ)	Length (m)	Width (m)	Thickness (m)
Silicon steel sheet	$2e11$ Pa	7650 kg/m^3	0.139	0.1	$6e-4$
Aluminum	$68e9$ Pa	2700 kg/m^3	0.139	0.1	$3e-3$

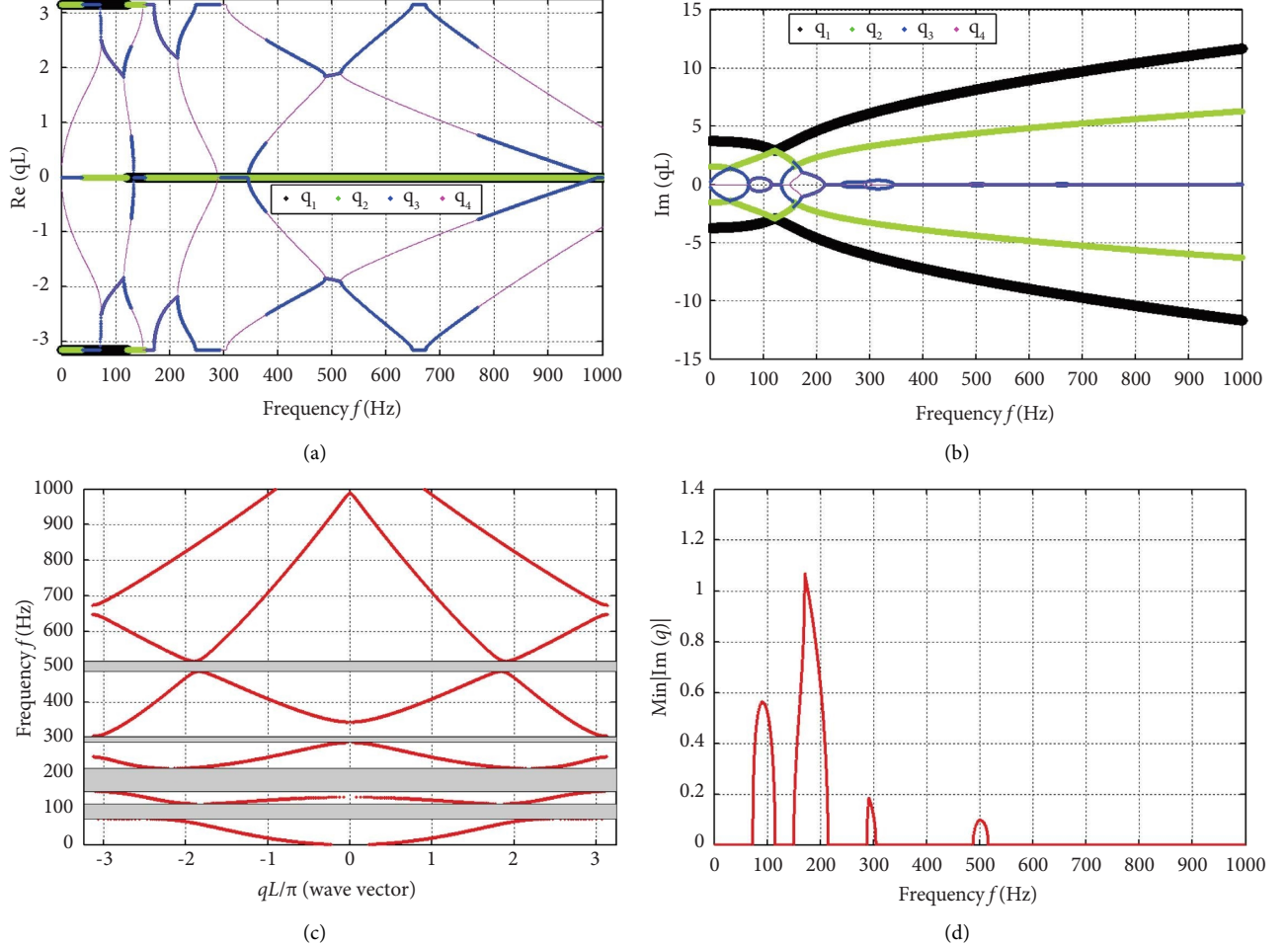


FIGURE 9: Bandgap structure of double-beam metamaterial: (a) real parts of wave number pairs, (b) imaginary parts of wave number pairs, (c) dispersion of double-beam metamaterial, and (d) minimum absolute value of attenuation constants.

and fourth bandgaps are generated by the blend of BS and LR mechanisms. In contrast, the third bandgap starts from 288 Hz to 305.2 Hz, which is attributed to Bragg scattering. Most importantly, all bandgaps denoted with grey areas in Figure 9(c) can effectively suppress the low frequency flexure vibrations at frequencies 100 Hz, 200 Hz, 300 Hz, and 500 Hz of silicon steel sheets for power transformer.

Figure 9(d) displays the attenuation constants within four bandgaps. It can be seen that the attenuation constants within the first and second bandgaps are relatively large, which means the low frequency flexure vibrations travelling cross these bandgaps will be attenuated dramatically. Whereas, the attenuation constants in third and fourth bandgaps are small and the low frequency vibration of silicon steel sheet can be suppressed as giving enough time.

3.3. Effects of Length L on the Bandgap Structure. Giving a view to the dispersion relation in equation (34), it is a function of the length L of the unit cell. Thus, the effects of length L on the characteristics of bandgaps are discussed in Figure 10. As the length L of the unit cell of the double-beam metamaterial increases from 0.12 m to 0.145 m, the dispersion curves move to low frequency region, and the width of each bandgap is reduced. The dispersion curve lied between the first two bandgaps is so flat that is helpful for controlling the low frequency vibration of transformers. For $L = 0.12$, 0.139, or 0.145, the width of bandgap of each case decreases as frequency goes up. Therefore, the low frequency vibration bandgap can be obtained by tuning length L .

Figure 10(b) also shows the variation of attenuation constants with respect to the length L . As length L increases, the lower and upper edge frequencies of each bandgap

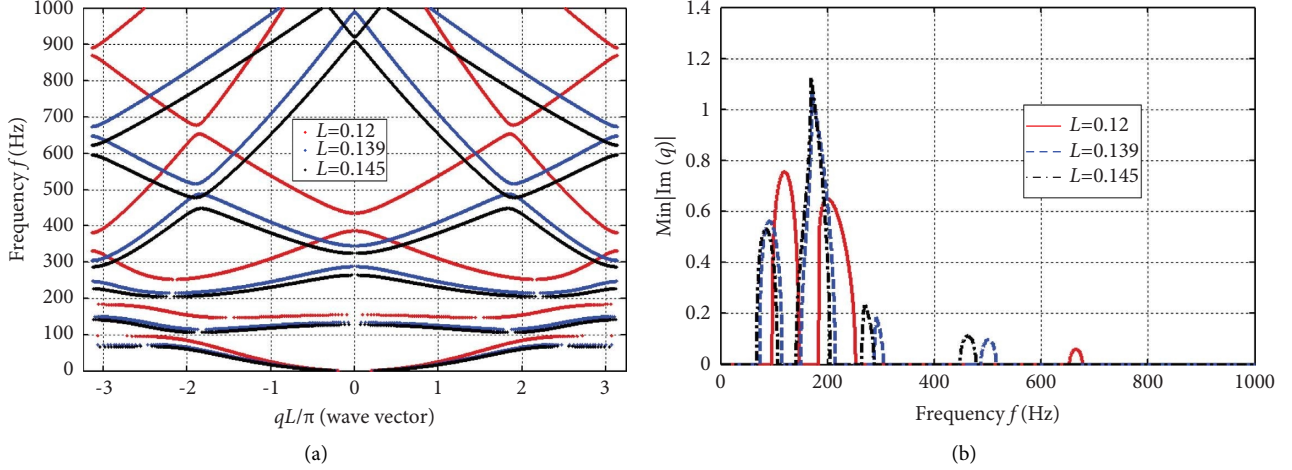


FIGURE 10: Effects of length L on bandgaps of the double-beam metamaterial: (a) effects of length L on bandgap structures and (b) effects of length L on attenuation constants.

moves to the low frequency region, which results in the position of each bandgap moving to the low frequency region as well. The attenuation constants of each bandgap in low frequency region are larger, which means these bandgaps can quickly attenuate low frequency flexure vibration of iron core. Whereas, the attenuation constants of high frequency bandgaps are small, thus, the vibration within these high frequency bandgaps can also be damped as long as there is enough time. Therefore, the bandgap can be tuned by optimizing the length L of the unit cell.

3.4. Effects of Stiffness on the Bandgap Structure. Since the dynamic coupling between the silicon steel sheet and aluminum beams is created by BQZSS, the intensity of coupling plays an important role in forming bandgaps. Hence, the effects of stiffness k_1 of BQZSS on the characteristics of bandgaps are analyzed in Figure 11. The BQZSSs made of PA12-I, PA12-II, and PA12-III in Section 2.2 are employed to couple the silicon steel sheet beam and aluminum beam. As stiffness k_1 increases, the edge frequencies of each bandgap increase, which results in the bandgaps moving to high frequency region. Besides, an almost flat dispersion curve is located between the first two bandgaps.

The attenuation constants of the double-beam metamaterial are also illustrated in Figure 11(b). When stiffness k_1 increases, the attenuation constants within the second, third, and fourth bandgaps increase gradually. Whereas, the attenuation constant in the first bandgap will decrease when k_1 goes up. Moreover, the lower and upper edge frequencies of each bandgap increase with the increase of k_1 . Hence, choosing an optimal stiffness k_1 is good for suppression of low frequency flexure vibration of iron core.

3.5. Parameters of Double Beams on the Bandgap Structure. The bandgap structures of the double-beam metamaterial are also determined by the parameters of two beams. According to equations (12)–(15), the characteristics of flexural wave travelling through the unit cell mainly depend

on the structural parameters. Once the materials of two beams are selected as silicon steel sheet and aluminum, respectively, the dynamics of the system can be tuned with moment of inertia I_i and the cross-sectional area A_i . Herein, the dimensions of aluminum beam remains unchangeable, and the ratio $\beta = \beta_2/\beta_1$ is defined to investigate the effects of geometric parameters on bandgaps, where $\beta_2 = \sqrt[4]{E_2 I_2 / \rho_2 A_2}$ and $\beta_1 = \sqrt[4]{E_1 I_1 / \rho_1 A_1}$. By tuning β from 1.32 to 1.85 as shown in Figure 12, the variation of the bandgap structure is displayed.

As β increases from 1.32 to 1.85, the lower and upper edge frequencies of each dispersion curve decrease, which yields the low frequency bandgap for iron core of transformers. Besides, the width of each bandgap is increasing with the increase of β . Interestingly, there is also a flat dispersion curve existing between the first two bandgaps. The effects of β on attenuation constants are also investigated in Figure 12(b). As β increases, the attenuation constant becomes larger and move to the low frequency region. Thus, a larger β has more advantages for low frequency flexural vibration of iron core.

4. Numerical Verification of Wave Transmission

In order to investigate the vibration transmittance properties of the double-beam metamaterial, the frequency response function (FRF) of the metamaterial with finite 75 unit cells has been calculated. As shown in Figure 13, the beam4 and combine14 elements are utilized to set up the finite element models of beams and BQZSS respectively, and two ends of the beam system are simply supported. The physical and geometrical parameters of two beams as well as the length L of unit cell are the same as discussed in the previous section. The stiffness coefficients of PA12-I in Table 3 are selected for the following analysis. Two beams in Figure 13 are meshed with 97500 finite beam elements. To conduct harmonic response analysis in ANSYS software, a harmonic excitation force with amplitude of 500 N is applied at a node adjacent of the left

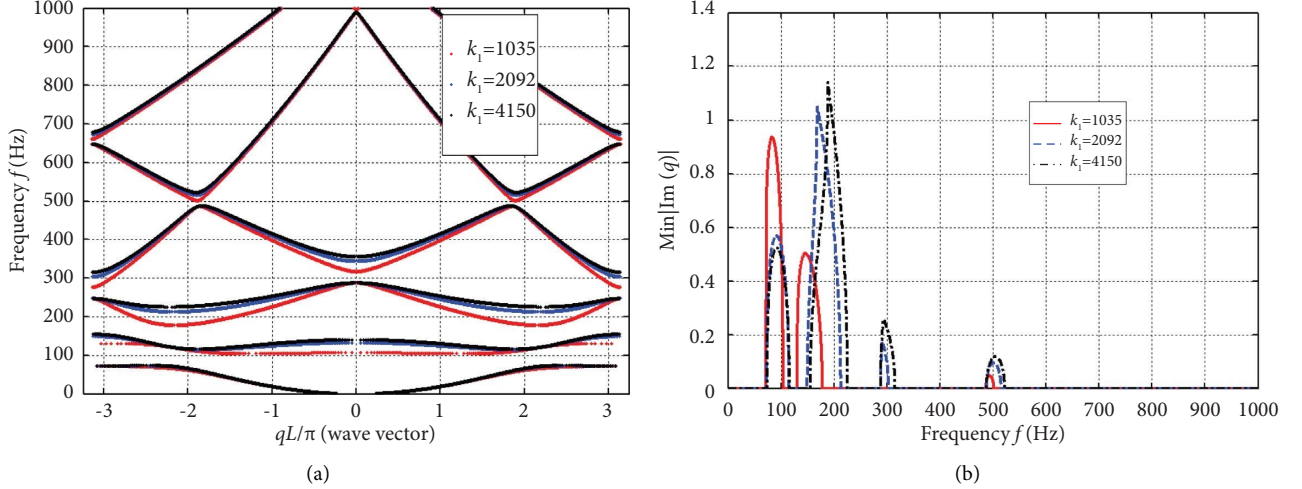


FIGURE 11: Effects of stiffness on bandgap of the double-beam metamaterial: (a) effects of stiffness on bandgap structures and (b) effects of stiffness on attenuation constants.

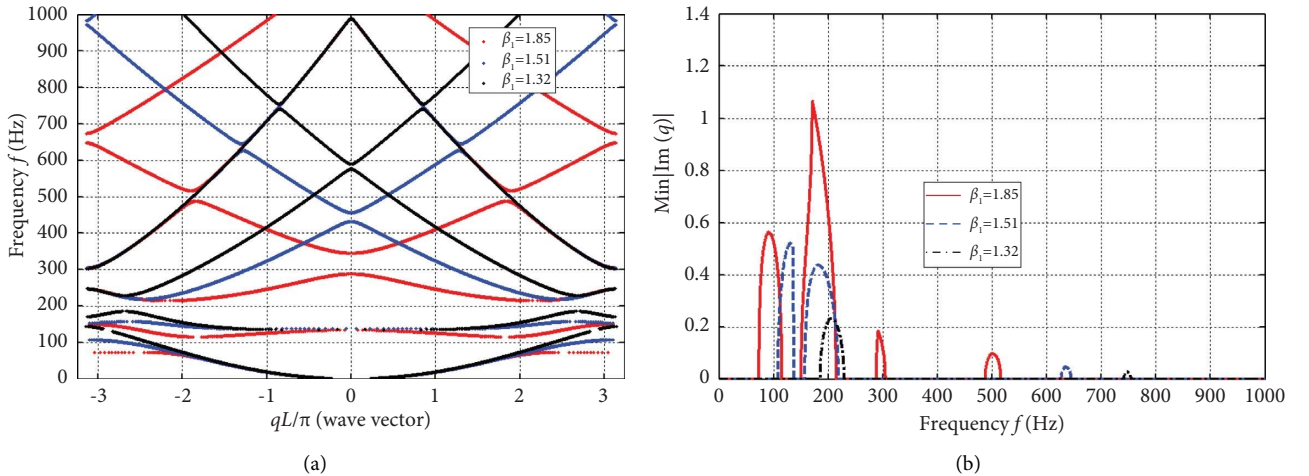


FIGURE 12: Effects of geometric parameters of beams on bandgap of metamaterial: (a) effects of geometric parameters on bandgap and (b) effects of geometric parameters on attenuation constant.

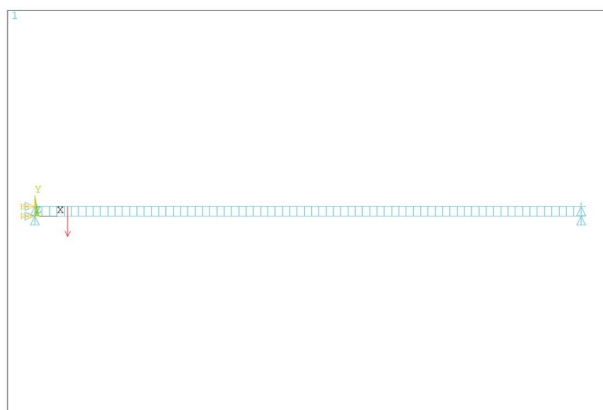


FIGURE 13: Finite element model of the double-beam metamaterial with 75 unit cells.

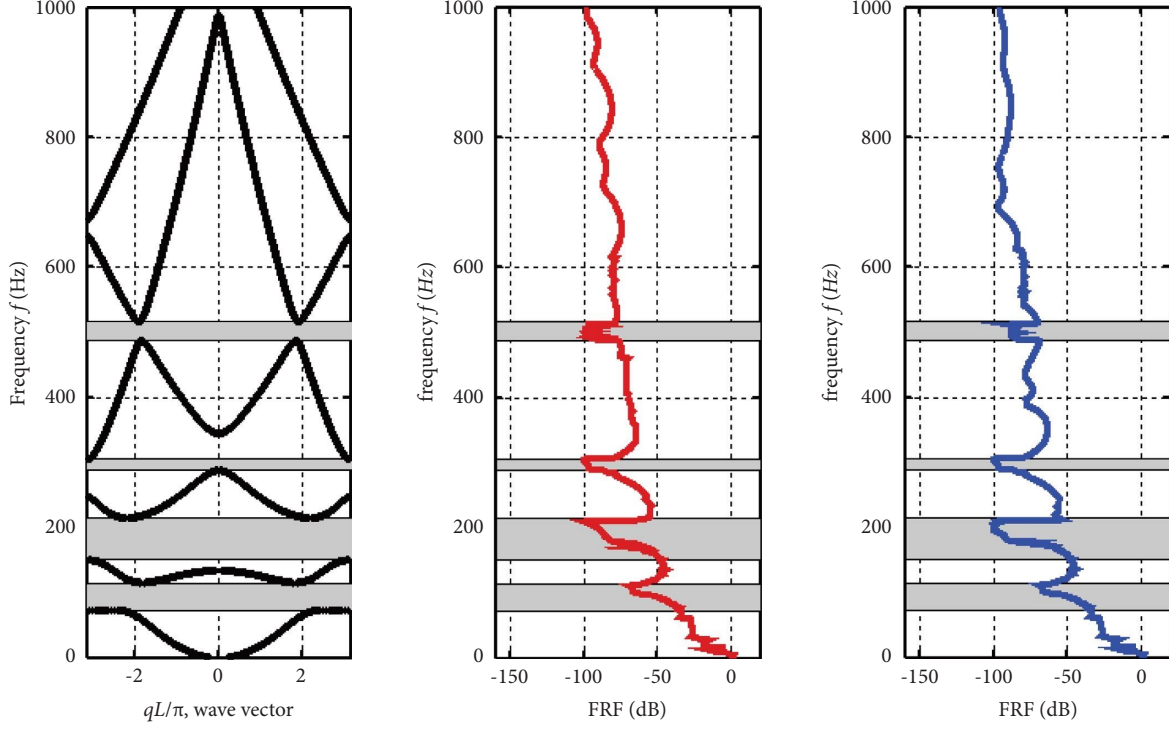


FIGURE 14: Comparison between the theoretical bandgaps and FRFs of the double-beam metamaterial.

support on the aluminum beam and the transverse displacement of the node adjacent of the right support for each beam is measured. Note that the node where the harmonic force applied is not the connection point of BQZSS, and the nodes where the transverse displacement measured are not the connection point of BQZSS. In addition, the damping coefficient of the system is assumed to be 0.01. Through the finite element analysis, the results are depicted in Figure 14.

As shown in Figure 14, the dispersion curves revealed in the left side are the theoretical results, while the red and blue curves plotted in the middle and the right sides are the frequency response functions of silicon steel sheet and aluminum beams, respectively. It is clear that the results of the theoretical bandgaps calculated in Section 3 have a good agreement with the FRFs computed in ANSYS, which proves the correctness of the theoretical model. The grey areas in Figure 14 are the bandgap regions, which result in the strong attenuation of both the beams. The attenuation strength in each region is consistent with the attenuation constants in Figure 9(d).

5. Conclusions

To suppress the low frequency flexural vibration and noise of iron core of power transformer caused by magnetostriction, a double-beam metamaterial constructed through coupling silicon steel sheet and aluminum beams with BQZSS is proposed. Unlike the traditional Bragg scattering or local resonance metamaterial using lattice or discrete resonators, the multiple low frequency bandgaps of the double-beam metamaterial are formed with dynamic coupling created by BQZSS, while each beam does not individually have bandgap. The dynamics of the unit cell is established in terms of Euler–Bernoulli beam theory,

and then, the dispersion relation is investigated with the consideration of boundary conditions and Bloch theorem. The effects of the parameters of two beam and BQZSS on the characteristics of bandgap are studied, which leads to BS-type bandgap and the blend of BS-LR type bandgap. Finally, the frequency response function of the double-beam metamaterial with a finite length is calculated to validate the theoretical bandgaps. The results show that the multiple low frequency vibration bandgaps at frequencies 100 Hz, 200 Hz, 300 Hz, and 500 Hz can be obtained for the suppression of main flexural vibration components of power transformer, and tuning the geometric parameters of two beams, length L of unit cell and stiffness of BQZSS can modify the bandgap structure by opening or closing gaps. Hence, the double-beam metamaterial proposed and offers a new control approach for low frequency vibration and noise of power transformer.

Data Availability

The data used to support the findings of this study are included within the article.

Conflicts of Interest

The authors declare that there are no conflicts of interest regarding the publication of this paper.

Acknowledgments

This work was supported by the Scientific and Technological Project of State Grid Smart Grid Research Institute Co., Ltd. (Grant No. 525500200050) and the National Natural Science Foundation of China (Grant No. 12002114).

Supplementary Materials

The supplementary document is the coefficient T_j ($j = 1 \sim 4$) in equations (33) and (34). (Supplementary Materials)

References

- [1] C.-fang Wang and Du. Tian-cang, "A reflection on the embarrassment of city substation addressing and its countermeasure," *Management*, vol. 24, no. 2, pp. 42–44, 2008.
- [2] Y. Wang, H. Jin, X. Cai, P. Gong, and X. Jiang, "Study on the sound radiation efficiency of a typical distribution transformer," *IEEE Access*, vol. 9, pp. 125151–125157, 2021.
- [3] Ji. Sheng-chang, Yu-hang. Shi, F. Zhang, and W.-feng Lu, "Review on vibration and noise of power transformer and its control measures," *High Voltage Apparatus*, vol. 55, no. 11, pp. 1–17, 2019.
- [4] H. Jingzhu, L. Dichen, L. Qingfen, Y. Yang, and L. Shanshan, "Electromagnetic vibration noise analysis of transformer windings and core," *IET Electric Power Applications*, vol. 10, no. 4, pp. 251–257, 2016.
- [5] H. Xia, K. Yang, Y. Ma, Y. Wang, and Y. Liu, "Noise reduction method for acoustic sensor arrays in underwater noise," *IEEE Sensors Journal*, vol. 16, no. 24, pp. 8972–8981, 2016.
- [6] B. Widrow, J. R. Glover, J. M. McCool et al., "Adaptive noise cancelling: principles and applications," *Proceedings of the IEEE*, vol. 63, no. 12, pp. 1692–1716, 1975.
- [7] X. Zhao, Z. Shuai, Y. Zhang, and Z. Liu, "Research on design method of metamaterial sound field control barrier based on transformer vibration and noise," *Energy Reports*, vol. 8, pp. 1080–1089, 2022.
- [8] L. Jiang-tao, *Research on the Key Technology of Active Noise Control for Power Transformer*, Wuhan University, Wuhan, China, 2012.
- [9] Yu. Wang and J.-wang. Zhao, "Analysis of oil-immersed power transformers noise and its countermeasure," *Power environmental protection*, vol. 3, pp. 45–47, 2008.
- [10] J.-zhu. Hu, L. Di-chen, M. Qing-fen, Y. Yang, and L. Shanshan, "Substation noise reduction effect of barrier and analysis of influencing factors," *Engineering Journal of Wuhan University*, vol. 50, no. 1, pp. 75–80, 2017.
- [11] D. Liu, B. Du, M. Yan, and S. Wang, "Suppressing noise for an HTS amorphous metal core transformer by using micro perforated panel absorber," *IEEE Transactions on Applied Superconductivity*, vol. 26, no. 7, pp. 1–5, 2016.
- [12] S. Wang, J. Tao, X. Qiu, and IS. Burnett, "A natural ventilation window for transformer noise control based on coiled-up silencers consisting of coupled tubes," *Applied Acoustics*, vol. 192, Article ID 108744, 2022.
- [13] L. Zhang, J. Tao, and X. Qiu, "Active control of transformer noise with an internally synthesized reference signal," *Journal of Sound and Vibration*, vol. 331, no. 15, pp. 3466–3475, 2012.
- [14] T. Zhao, J. Liang, L. Zou, and L. Zhang, "A New FXLMS Algorithm With Offline and Online Secondary-Path Modeling Scheme for Active Noise Control of Power Transformers," *IEEE Transactions on Industrial Electronics*, vol. 64, no. 8, pp. 6432–6442, 2017.
- [15] Yu-lan. Zhang, "Application of rubber vibration isolator in realizing transformer vibration and noise reduction," *Occupation*, no. 20, p. 109, 2013.
- [16] G.-xu. Dong, Yu-cheng. Liu, Q. He et al., "Nonresonant response of quasi-zero stiffness platform for power transformer," *Chinese Journal of Applied Mechanics*, vol. 37, no. 6, pp. 2463–2469, 2020.
- [17] Li. Wen-peng, L. Hai-bo, C.-cheng. Cao et al., "Investigation on the vibration isolation and noise reduction of dual-nonlinearity isolation system for transformer," *Mechanical Science and Technology for Aerospace Engineering*, vol. 39, no. 2, pp. 1836–1843, 2020.
- [18] J. Zhou, H. Cao, Y. Chang et al., "High-efficiency vibration isolation for a three-phase power transformer by a quasi-zero-stiffness isolator," *Shock and Vibration*, vol. 2021, Article ID 5596064, 11 pages, 2021.
- [19] H. Cao, G. Li, W. Zhang, X. Wu, L. Lu, and S. Hu, "Suppression method of vibration and noise for power transformer using tuned mass damper [C]. IOP conference series: earth and environmental science," *IOP Conference Series: Earth and Environmental Science*, vol. 440, no. 3, Article ID 032048, 2020.
- [20] T.-zheng. Wang, C. Zhang, X.-zhe. Zhao, K. Yin-zhu, L. Guo-qiang, and B.-guo. Tang, "Noise reduction method with acoustic metamaterials based on noise characteristics of power transformer," *High Voltage Apparatus*, vol. 55, no. 11, pp. 277–282, 2019.
- [21] X.-zhe. Zhao, L. Guo-qiang, and D. Xia, "Application of hybrid coiled acoustic metamaterials in low frequency sound insulation," *Journal of Shanxi Normal University (Philosophy and Social Sciences edition)*, vol. 47, no. 6, pp. 100–104, 2019.
- [22] X. Zhao, G. Liu, C. Zhang, D. Xia, and Z. Lu, "Fractal acoustic metamaterials for transformer noise reduction," *Applied Physics Letters*, vol. 113, no. 7, Article ID 074101, 2018.
- [23] L. Li, R. Xi, H. Liu, and Z. Lv, "Broadband polarization-independent and low-profile optically transparent metamaterial absorber," *Applied Physics Express*, vol. 11, no. 5, Article ID 052001, 2018.
- [24] T. Wang, T. Jin, and Z. Lu, "Research on active noise control method compensating for acoustic metamaterial noise barrier in transformer noise reduction," in *Proceedings of the 2018 IEEE 2nd International Electrical and Energy Conference (CIEEC)*, pp. 648–652, IEEE, Beijing, China, November 2018.
- [25] M. Yuchao, M. Juan, X. Ke, L. Xiang, and S. Xinbo, "Material Parameters Acquisition and Sound Insulation Performance analysis of Membrane-type Acoustic Metamaterials Applied for Transformer," *E3S Web of Conferences*, vol. 136, Article ID 01031, 2019.
- [26] N. Sharafkhani, *A Helmholtz Resonator-Based Acoustic Metamaterial for Power Transformer Noise Control*, pp. 1–7, Acoustics, Australia, 2021.
- [27] Y. R. Ye, X. P. Wang, T. N. Chen, and YY. Chen, "Step-by-step structural design methods for adjustable low-frequency sound insulation based on infinite plate-type acoustic metamaterial panel," *Modern Physics Letters B*, vol. 34, no. 21, Article ID 2050220, 2020.
- [28] N. P. Mastriola, J. T. Dreyer, and R. Singh, "Analytical and experimental characterization of nonlinear coned disk springs with focus on edge friction contribution to force-deflection hysteresis," *Mechanical Systems and Signal Processing*, vol. 91, pp. 215–232, 2017.
- [29] M. Y. Wang and X. Wang, "Frequency band structure of locally resonant periodic flexural beams suspended with force-moment resonators," *Journal of Physics D: Applied Physics*, vol. 46, no. 25, Article ID 255502, 2013.